UC Riverside
BCOE Research

Title

ECEF Position Accuracy and Reliabilityin the Presence of Differential Correction LatencyPhase B Technical Reportfor Sirius XM

Permalink

https://escholarship.org/uc/item/135578mw

Authors

Rahman, Farzana
Aghapour, Elahe
Farrell, Jay A.

Publication Date

2019-06-19

ECEF Position Accuracy and Reliability
in the Presence of Differential Correction Latency

Phase B Technical Report
for Sirius XM

Farzana Rahman, Elahe Aghapour and Jay A. Farrell
Department of Electrical and Computer Engineering,
University of California, Riverside, 92521.
{frimi, eaghapour, farrell}@ece.ucr.edu

Executive Summary

Many applications, including connected and autonomous vehicles, would benefit from navigation technologies reliably achieving sub-meter position accuracy with high reliability on moving platforms. Commercial on-vehicle implementation of Earth-referenced positioning at submeter accuracy with 99% probability would require widely and reliably available differential corrections; however, such corrections delivered on a nationwide or global scale via satellite systems will incur latency between their time-of-applicability and their time-of-reception at the vehicle.

Phase 1 of this project presented a differential correction computation methodology designed to be robust to latency and studied position accuracy as a function of differential correction latency for stationary receivers [1]–[3]. The study showed that submeter accuracy at 95% probability was achievable when a sufficient number and diversity of satellites were available.

This report summarizes the conclusions of the Phase 2 of the work performed by University of California, Riverside (UCR). There were two main goals for this effort. For moving platforms, Phase 2 investigates:

1) the feasibility of achieving meter-level positioning accuracy on at least 95% of epochs using Global Navigation Satellite System (DGNSS) based state estimation; and,
2) the sensitivity of that positioning accuracy to communication latency.

The study uses the utilizes the local based station design presented in [1].

The study presents and experimentally analyzes two state estimation approaches suitable for moving platforms. The Position, Velocity, Acceleration (PVA) approach uses DGNSS data only within a Kalman filter framework. The Inertial Navigation System (INS) approach uses DGNSS and inertial measurement data within an extended Kalman filter implementation. Section VII shows that both approaches have performance exceeding the SAE J2945 specification (1.5 meter horizontal accuracy and 3.0 meter vertical accuracy at 68%) with PVA achieving 1m horizontal at 90% and 2 m vertical accuracy at 95% while the INS approach using a consumer-grade IMU achieves 1m horizontal at 98% and 2 m vertical accuracy at 95%.

Section VIII presents an analysis of position estimation accuracy, for moving platforms, as a function of communication latency, which shows that, using the DGNSS correction computation approach presented in [1], position estimation accuracy is robust to correction latency exceeding 500 seconds.

The results herein used a local base station approach. National or global implementations would be more efficient using networks of base stations working collaboratively to estimate parameters usable by user receivers to reconstruct corrections. Such methods are the focus of Phase 3 of this study.

This study focuses on single frequency, single constellation results. The availability of multiple constellations and multiple frequencies per constellations will facilitate compensation of ionospheric error, accommodation of outliers, and accommodation of multipath, while still having a set of satellites with appropriate geometry to reliably achieve the performance specification.

CONTENTS

I. INTRODUCTION

Over the last several decades, Global Navigation Satellite Systems (GNSS) [4]–[7] have become dominant for personal and vehicular position determination for routing applications. For such applications, standard GNSS accuracy of about 10 m has typically been sufficient.

A new generation of applications (e.g., autonomous vehicles, connected vehicles, and driver's assistance [8]–[11]) are placing much stricter position accuracy and reliability specifications on navigation systems than was previously required. Specifically stated specifications (e.g., SAE J2945 [12]) require horizontal and vertical position accuracy of 1.5 m and 3 m with 68% probability, respectively. The FHWA, state DOTs, and auto manufacturers are investigating connected and autonomous highway vehicle applications which will benefit from real-time, Earth Centered Earth Fixed (ECEF) position estimates accurate to sub-meter level at 95% probability. Pilot projects are ongoing in at least three locations [9]–[11]. The objectives of these projects include improving roadway network safety and throughput, while decreasing emissions impact.

Commonly cited differential GNSS (DGNSS) position accuracy levels are 1-3 meters [13]. The lower end of this range approaches the desired sub-meter specification, if this accuracy can be achieved with sufficient reliability and if it is not sensitive to DGNSS correction communication latencies. This report presents local DGNSS correction and platform state estimation algorithms, with experimental results that exceed the specification stated in the previous paragraph.

Navigation systems achieving these accuracy and reliability specifications have not yet been demonstrated. For a national scale of implementation, topics of interest include: communication physical layers, network design for real-time applications, position error sensitivity to communication latency, and estimation algorithms to achieve the accuracy specification.

This report studies the achievable accuracy of alternative estimation algorithms and the position estimation accuracy as a function of communication latency. Section II contains a literature review. Section III presents notation and background related to the measurement and models. Section IV discusses the differential correction latency compensation approach and double difference measurements. Section V presents the state estimation methods that are used herein. Because the platform is moving, a state vector must be defined that includes position, for each approach. Section VI discusses the experimental data that will be used for this study. Section VII presents the position estimation results when the communication latency is zero. Section VIII presents the position estimation results as a function of communication latency. Section IX studies the effect of outliers on the state estimation results.

II. RELATED WORK

Position determination by standard GNSS positioning [14]–[16] as well as DGNSS [17]–[19] are both very well researched areas. The extensive literature presents position estimation theory, estimation algorithms, and experimental results that illustrate alternative modeling choices and their impact on performance and reliability [20]–[22].

A challenge in DGNSS positioning is the sensitivity of position error to communication latency. In the era of selective availability (SA) there were many investigations to characterize sensitivity to DGNSS correction latency [23]–[27]. Due to the design of SA, as intended, the correction error and hence the position error grew rapidly over tens of seconds. Until recently, the literature lacked studies of real-time positioning performance as a function of correction latency in the post-SA era. For stationary platforms, this issue was studied in [2]. This report presents an analysis of positioning accuracy as a function of communication latency for moving platforms.

In DGNSS the dominant error source is the multipath. The literature provides several methods to address the issue. In [28], the authors introduced a narrow correlator tracking loops that provided a 20-50% reduction in multipath error effects for the L1 pseudorange measurement. In [29], [30], multipath error modeling is addressed using dual frequency carrier phase measurements in a GNSS antenna array system. A choke ring antenna [31] is another option. None of these technologies have yet arrived in commercial products at a price point suitable for automobile applications. Alternatively, many implementations augment one (or more) multipath state per satellite to the state vector. Use of Doppler improves positioning performance by estimating the velocity [32]–[35]. A less well understood benefit of the Doppler measurement is that it enhances the degree-of-observability of the multipath states. This topic with a simple example is discussed in [1], [2].

Articles [1], [2] presented a differential correction computation algorithm that was demonstrated in experiments to be robust to communication latency exceeding 500 s; however, the analysis of positioning accuracy and latency sensitivity therein was limited to stationary data. This report extends that analysis to moving platforms. Two state estimation approaches are presented for the moving platform, one using DGNSS only and one combining DGNSS and IMU data. This report also demonstrates that, on the moving platform, meter level horizontal position accuracy is achieved for 98% of the samples with two meter vertical accuracy achieved on 97% of the samples. This level of performance exceeds the requirements of SAE specification J2945.

III. BACKGROUND AND PROBLEM STATEMENT

This section introduces notation and GNSS measurement models. For additional information on GNSS, see [14]–[16], [20], [21].

A. GNSS Background

GNSS receivers provide three measurements: pseudorange, Doppler, and carrier phase. At present, these signals are available to civilians only on the L1 frequency. In the near-term, low-cost consumer receivers are expected to provide additional measurements from multiple constellations and at multiple frequencies (i.e., L1, L2, and L5 for GPS). The methods

discussed herein generalize to multiple frequencies and constellations with only minimal algorithmic changes. Additional frequencies and multiple constellations will further enhance performance. For example, measurements at multiple frequencies will improve estimation of ionospheric delay. Multiple constellations and multiple frequencies will greatly increase the number of measurements allowing attenuation of multipath and outlier effects. This study focuses on L1 pseudorange and Doppler measurements for the GPS constellation.

B. Notation

To clearly distinguish between models and computations, this article will use two different symbols. The symbol $\doteq$ indicates that the equation is a model. Models are used to analyze, understand, and physically interpret measurements, often with the goal of designing algorithms to estimate quantities that are of interest (e.g., position). The symbol $=$ indicates that an equation represents an actual algorithmic calculation.

When it is necessary to represent both the actual and computed versions of a variable, x will represent the actual value while $\hat{x}$ will represent the computed value. For example, p^s represents the actual position of satellite s while $\hat{p}^s$ represents the position of satellite s computed from the available ephemeris data.

C. GNSS Measurement Models

The pseudorange measurement model is

$$\rho_r^s \doteq R(p_r, p^s) + ct_r - ct^s + I^s + T^s + M_r^s + \eta_r^s, \quad (1)$$

where the range between the receiver location p_r and the satellite location p^s is

$$R(p_r, p^s) = |p_r - p^s|. \quad (2)$$

The symbol ct_r represents the receiver clock bias, ct^s is the satellite clock bias after ephemeris corrections, I^s is ionospheric error, T^s is tropospheric error, M_r^s is multipath error, and $\eta_r^s \sim \mathcal{N}(0, R_p^s)$ is white random noise affecting the pseudorange measurement. Ephemeris error is accounted for later.

The Doppler D_r^s measurement model is

$$\lambda D_r^s \doteq h^s \cdot (v_r - v^s) + cb_r - cb^s + \varepsilon_r^s \quad (3)$$

where the line-of-sight vector from satellite s to receiver r is

$$h^s = \frac{p_r - p^s}{|p_r - p^s|}. \quad (4)$$

The symbols v_r and v^s represent the receiver and satellite antennae velocity vectors, cb_r and cb^s are the receiver and satellite clock drift rates, and $\varepsilon_r^s \sim \mathcal{N}(0, R_d^s)$ is white random measurement noise affecting the Doppler measurement.

D. GNSS Measurement Errors

The pseudorange measurement has 7 types of errors, (see [36], and Sections 1.2-1.3 of [13]). They can be classified into two categories:

- *Common-mode errors* (ephemeris, satellite clock bias, ionosphere, troposphere) are common to all receivers in the same vicinity.

- *Noncommon-mode errors* (receiver clock bias, multipath, receiver noise) are different for each receiver.

Differential GNSS processing methods are defined to reduce the effects of common-mode errors [17]–[19] on the position estimates.

E. Problem Statement

This report presents position estimation algorithms applicable to moving receivers using either GNSS or GNSS and inertial measurements. It also analyzes the extent to which these algorithms achieve the position accuracy and reliability specifications currently envisioned for driver assistance, connected vehicle, and autonomous vehicle applications [12]. Of particular interest is the sensitivity of the positioning accuracy to latency in the communication of GNSS differential corrections to the roving vehicle.

IV. DIFFERENTIAL GNSS CORRECTION

Section IV-A and IV-B discuss DGNSS techniques and delineate various issues that must be addressed to achieve sub-meter positioning accuracy. The DGNSS correction computation approach, originally presented in [1], was designed to accommodate communication latency. It is reviewed in Section IV-C and will be used for all results herein, along with double-differencing as discussed in Section IV-D.

A. DGNSS Correction Approaches

All DGNSS approaches use at least one base station with a high quality receiver and antenna located at a mechanically stable and known location p_b. Due to the antenna location being stationary and known, the DGNSS approach can estimate corrections for roving receivers, enabling significant enhancement in rover position estimation accuracy, assuming that the corrections can be communicated to the rovers in a time-effective manner.

DGNSS can be implemented on local, regional, or global scales. Local DGNSS approaches are the easiest to understand and are currently planned to be used for the Department of Transportation pilot projects described in [9]–[11].

The standard local approach is described in detail in Section IV-B. Regional and global approaches utilize a network of GNSS receivers. The measurements from throughout the network are combined to estimate correction information that is broadcast to users, such that each user can reconstruct a local correction [37], [38]. For commercial DGNSS applications on a global scale, network DGNSS methods are likely to be the most feasible for a few reasons. First, the number of base stations is significantly reduced relative to local approaches implemented worldwide. Second, a single entity responsible for the network of base stations can implement measures to ensure and verify integrity. Third, commercial entities utilizing the corrections (e.g., car manufacturers) could interact with a single standard (e.g., data format and communication physical layer) globally rather than numerous local standards.

The collection of data from remote base receivers, computation and verification of corrections, and communication

of corrections to users result in latency ℓ between the time-of-applicability t_0 and the time that it is actually used $t_0 + \ell$. Robustness to communication latency is critical.

A primary goal of this study is to evaluate the sensitivity of positioning accuracy to communication latency. For the purpose of this study, it is sufficient to utilize local corrections. The local approach used in this paper, described in Section IV-C, is a variant of the RTCM standard [17].

For the approach herein, the correction convergence time at the rover is zero seconds, once the base station message is received. For alternative approaches, such as those based on precise point positioning [13], [39], [40], the convergence time is non-zero, so the results of this study would not be applicable.

B. Standard Local DGNSS Corrections

This section discusses a local base station algorithm [1] that is essentially compatible with the RCTM standard [17]. The local base station position p_b is assumed to be known to centimeter accuracy, so that its error is neglected herein.

At time t the base station algorithm computes

$$\tilde{c}^s(t) = \rho_b^s(t) - R(p_b, \hat{p}^s(t)) - c\hat{t}_b(t) + c\hat{t}^s(t) \qquad (5)$$

where ρ_b^s is the base pseudorange measurement. The computed range from the known base location p_b to the satellite location $\hat{p}^s$ computed using the ephemeris data is $R(p_b, \hat{p}^s) = |p_b - \hat{p}^s|$. The satellite clock bias $c\hat{t}^s$ is also computed from ephemeris data. The symbol $c\hat{t}_b(t)$ represents an estimate of the base receiver clock bias. The estimated base receiver clock bias is only removed to reduce the magnitude of the correction and will not affect the positioning error.

The model for $\tilde{c}^s(t)$ is

$$\begin{aligned} \tilde{c}^s(t) &\doteq I^s(t) + T^s(t) + E^s(t) - c\delta t^s(t) \\ &+ c\delta t_b + M_b^s(t) + \eta_b^s(t) \end{aligned} \qquad (6)$$

where $E^s = R(p_b, p^s) - R(p_b, \hat{p}^s)$ is satellite ephemeris error, $c\delta t^s = ct^s - c\hat{t}^s$ is residual satellite clock bias and $c\delta t_b = ct_b - c\hat{t}_b$ is residual receiver clock bias. Note that all of the terms on the right-hand side of eqn. (6) are unknown. The goal is that the broadcast correction to the rover should allow accurate prediction of the common mode error

$$I^s(t) + T^s(t) + E^s(t) - c\delta t^s(t),$$

while being minimally influenced by the base station non-common mode error

$$M_b^s(t) + \eta_b^s(t).$$

Eqn. (6) shows that $\tilde{c}^s(t)$ contains both common and non-common mode errors; therefore, additional processing is desirable.

C. Approach to Decrease Mulipath and Latency Effects

Each noncommon-mode error source is correlated over only a few minutes whereas the common-mode error sources are correlated over several hours. Due to this frequency separation, various forms of low-pass filtering should attenuate the affects of the noncommon-mode errors.

Before filtering, it is useful to consider the ionospheric delay. When the rate of change of the ionospheric delay is high, a low-pass filtered correction would lag the present value of $\tilde{c}^s(t)$. The ionospheric delay has trends that are largely predictable using GNSS satellite data available at each base and rover. Therefore, the predictable portion of these terms is removed prior to filtering and added back into the filtered results.

Let $\hat{I}^s$ represents the ionosphere delay computed using GNSS satellite data. Subtracting this predicted ionospheric delay produces the new computed variable

$$\tilde{d}^s(t) = \tilde{c}^s(t) - \hat{I}^s(t). \qquad (7)$$

The model for $\tilde{d}^s(t)$ is

$$\begin{aligned} \tilde{d}^s(t) &\doteq \delta I^s(t) + T^s(t) + E^s(t) - c\delta t^s(t) \\ &+ M_b^s(t) + \eta_b^s(t) \end{aligned} \qquad (8)$$

where $\delta I^s(t) \doteq I^s(t) - \hat{I}^s(t)$. The first line of eqn. (8) contains the desired signal for the corrections. These signals have very small changes in rate over long periods of time (i.e., many minutes). The second line of eqn. (8) contains the noncommon-mode errors. These errors change rapidly and are zero mean over several minutes. Therefore, to also attain the ability to predict corrections at future times, the form of low pass filter that we select is line-fitting.

At time t_0, the line $a_{t_0} + b_{t_0}(t - t_0)$ is fit to the data

$$\left\{ \tilde{d}(t) \text{ for } t \in [t_0 - L, t_0] \right\}.$$

The parameters $[a_{t_0}, b_{t_0}, t_0, IODE]$ are communicated to the rover, arriving at some time after t_0. The parameter $IODE$ ensures that the base and rover use the same issue of ephemeris data. For any time $t \geq t_0$, the rover computes the correction as

$$\hat{c}(t; t_0) = a_{t_0} + b_{t_0}(t - t_0) + \hat{I}^s(t). \qquad (9)$$

For position computations, the rover uses the DGNSS compensated pseudorange measurement:

$$\Delta \rho_r^s(t; t_0) = \rho_r^s(t) - \hat{c}(t; t_0). \qquad (10)$$

The correction latency is $l = (t - t_0)$. Assuming perfect cancellation of common-mode errors when $l = 0$ and elimination of the base multipath and receiver noise from the corrections, the DGNSS compensated pseudorange model (using $\hat{c}(t; t_0)$ at time t) is

$$\begin{aligned} \Delta \rho_r^s(t; t_0) &\doteq R(p_r(t), \hat{p}^s(t)) + ct_{rb}(t) \\ &+ (\hat{c}(t; t) - \hat{c}(t; t_0)) + M_r^s(t) + \eta_r^s(t). \end{aligned} \qquad (11)$$

The term $(\hat{c}(t; t) - \hat{c}(t; t_0))$ accounts for the error in prediction of the common-mode errors due to communication latency.

The remaining base clock error $c\delta t_b$ affects all satellites identically and is lumped into the receiver clock error as $ct_{rb} = ct_r - c\delta t_b$.

The DGNSS correction in eqn. (9) is designed to be robust to latency and base station multipath error. Figures showing the results of example base station calculations are included in an Appendix of [1]. Latency effects on both correction and positioning error are analyzed in Section VI.

D. Double-Differenced Measurement Model

DGNSS corrections compensate for the common-mode errors that affect the pseudorange measurement. The receiver clock biases can be eliminated by double differencing (See Section 8.8.3 in [20]). In double-differencing, one satellite, called the pivot satellite, has its differential measurement subtracted from all the others. This operation removes clock bias errors (i.e., two states from the model) at the cost of one fewer measurement per epoch and causing the noise on all double-differenced measurments per epoch to be correlated.

For correction latency, $l = 0$, the DGNSS compensated measurement model from eqn. (11) reduces to

$$\Delta\rho_r^s \doteq R(p_r, \hat{p}^s) + ct_{rb} + M_r^s + \eta_r^s, \tag{12}$$

where the time index t has been omitted for simplicity.

For the results herein, the pivot satellite (denoted as s_p) will be the one with the highest elevation angle. The double-differenced pseudorange measurement $\nabla\Delta\rho_r^s$ is computed as

$$\nabla\Delta\rho^s = \Delta\rho_r^s - \Delta\rho_r^{s_p}. \tag{13}$$

The corresponding measurement model is

$$\nabla\Delta\rho^s \doteq R(p_r, \hat{p}^s) - R(p_r, \hat{p}^{s_p}) + dM_r^s + d\eta_r^s, \tag{14}$$

where $dM_r^s = M_r^s - M_r^{s_p}$ and $d\eta_r^s = \eta_r^s - \eta_r^{s_p}$ are the time-correlated multipath and white measurement noise processes.

The single-differenced Doppler measurement is computed as

$$\lambda\Delta D_r^s = \lambda D_r^s + 1_r^s \cdot \hat{v}^s \tag{15}$$

which uses the ephemeris data to remove the portion of Doppler due to satellite motion (i.e., $1_r^s \cdot \hat{v}^s$). The line-of-sight vector from the satellite to the receiver is 1_r^s. It is also the case that $\frac{\partial R}{\partial p_r} = 1_r^s$, so that this vector will have a role in Section V-B. This vector is time varyint, due to the motion of the satellite and receiver antenna, but the subscript k is dropped to simplify the notation.

Based on eqn. (3) the single-difference Doppler model is

$$\lambda\Delta D_r^s \doteq 1_r^s \cdot v_r + cb_r + \varepsilon_r^s, \tag{16}$$

where the satellite velocity error term $(1_r^s \cdot \hat{v}^s - 1_r^s \cdot v^s)$ is negligible and has been dropped.

Performing the difference between satellites yields the double-differenced Doppler measurement is computed as

$$\lambda\nabla\Delta D^s = \lambda\Delta D_r^s - \lambda\Delta D_r^{s_p}, \tag{17}$$

which yields the measurement model

$$\lambda\nabla\Delta D^s \doteq (1_r^s - 1_r^{s_p}) \cdot v_r + d\varepsilon_r^s. \tag{18}$$

where $d\varepsilon_r^s = \varepsilon_r^s - \varepsilon_r^{s_p}$ is the white Doppler measurement noise that is correlated between satellites.

Define the vector of two measurements per satellite at epoch k as:

$$z_k^s = h^s(x_k) + \gamma_k^s, \tag{19}$$

where (dropping the subscript k from the time varying function h_k^s)

$$z_k^s = \begin{bmatrix} \nabla\Delta\rho_k^s \\ \nabla\Delta D_k^s \end{bmatrix} \text{ and } h^s(x) = \begin{bmatrix} R(p, \hat{p}_k^s) - R(p, \hat{p}_k^{s_p}) \\ (1_r^s - 1_r^{s_p}) \cdot v \end{bmatrix}$$

where receiver antenna position p and velocity v will be subvectors of the state vector x. The noise vector $\gamma_k^s \sim \mathcal{N}(0, R_z)$ with

$$R_z = \begin{bmatrix} R_p^s + R_p^{s_p} & 0 \\ 0 & R_d^s + R_d^{s_p} \end{bmatrix}.$$

The vector of measurements at epoch k corresponding to the model in eqn. (19) concatenates the measurements per satellite: $z_k = [z_k^1, \ldots, z_k^m]^\top$ where $h(x) = [h^1(x), \ldots, h^m(x)]^\top$.

V. POSITION ESTIMATION ON A MOVING PLATFORM

This section presents the position estimation algorithms that will be used for performance analysis herein.

A. Time Propagation Models

Two approaches to temporal propagation of the state are considered. The position, velocity, and acceleration (PVA) approach of Section V-A1 only uses GNSS measurements, while the INS approach of Section V-A2 also incorporates inertial measurements.

1) PVA Time Propagation Model: The PVA rover state is

$$x = [p^\top, v^\top, a^\top, M_r]^\top \in \mathbb{R}^{n_s}, \tag{20}$$

where $n_s = 9 + m$. The symbols $p, v, a \in \mathbb{R}^3$ represent the position, velocity and acceleration vectors. The analysis herein augments the standard PVA state vector [1], [20], [41] with a vector of multipath states $M_r \in \mathbb{R}^m$.

The discrete-time state is assumed to propagate as

$$x_k \doteq \Psi x_{k-1} + \Gamma \omega_{k-1}, \tag{21}$$

where $x_k = x(t_k)$, $t_k = kT$, where T is the time between measurement epochs, $\omega_k \sim \mathcal{N}(0, Q_d)$ and the matrices of the discrete-time state-space model are:

$$\Psi = \begin{bmatrix} \psi_v & 0 \\ 0 & \psi_M \end{bmatrix}, \quad \Gamma = \begin{bmatrix} \Gamma_v & 0 \\ 0 & \Gamma_M \end{bmatrix}, \text{ and } Q_d = \begin{bmatrix} Q_{d_v} & 0 \\ 0 & Q_{d_M} \end{bmatrix}.$$

The PVA model assumes that the acceleration vector is constant for all $t \in [t_{k-1}, t_k]$ (i.e., over each measurement epoch) and that its value is accurately modeled as a first-order discrete-time Markov process between measurement epochs. The parameters of the acceleration Markov process are assumed to be time-invariant.

The trade-off in the PVA approach is that there is no optimal set of model parameters uniformly applicable over all epochs. Nevertheless, the designed must choose a set of model parameters at design time. For epochs over which the selected

model is accurate, the PVA approach will perform well, perhaps even optimally. Over other epochs, the performance may deteriorate. Herein, the model parameters of the PVA and multipath states are tuned for a moving platform with moderate acceleartion correlated over a few seconds. The details of the model and its parameters are discussed in [1].

The PVA state estimate is time-propagated as

$$\hat{x}_k^- = \Psi \hat{x}_{k-1}^+, \tag{22}$$

where the superscript '$-$' and '$+$' denote the values just before and after incorporating the GNSS measurements at time k. The error state covariance matrix is propagated as

$$P_k^- = \Psi P_{k-1}^+ \Psi^\top + \Gamma Q_d \Gamma^\top. \tag{23}$$

The index k counts over GNSS measurement times $t_k = kT$. GNSS receivers allow the user to select T over a wide range from 0.02 seconds to infinity. The tradeoff is that the validity of the PVA model improves for smaller T, but the assumption of GNSS white measurment noise becomes more valid as T increases. In this article, $T = 1$ second.

2) INS Time Propagation Model: The INS rover state is

$$x = [p^\top, v^\top, q^\top, b_a^\top, b_g^\top, M_r^\top]^\top \in \mathbb{R}^{n_s}. \tag{24}$$

where $n_s = 16 + m$ and m is the number of GNSS satellites available. The symbols $p, v, b_a, b_g \in \mathbb{R}^3$ represent the position, velocity, accelerometer bias and gyro bias vectors, while $q \in \mathbb{R}^4$ is the attitude quaternion, and $M_r \in \mathbb{R}^m$ is the multipath bias state vector with one element per satellite.

The kinematic model for the continuous-time propagation of the vehicle state is:

$$\dot{x}(t) \doteq f(x(t), u(t)) \tag{25}$$

where the specific form of the function f can be found in many references, e.g., [20]. The vector $u \in \mathbb{R}^6$ denotes the IMU sensor measurements: specific force vector and angular rate vector.

The IMU measurements occur in discrete-time with sample period $\tau \ll T$. The IMU discrete-time measurements are modeled as

$$\tilde{u}(\tau_{k,i}) \doteq u(\tau_{k,i}) + b_u(\tau_{k,i}) + \omega_u(\tau_{k,i}) \tag{26}$$

where $\omega_u(\tau_{k,i}) \sim \mathcal{N}(0, Q)$ and the sensor bias vector $b_u = [b_a^\top, b_g^\top]$ is modeled as a first-order Markov process. Let $\tau_{k,i} = t_k + i\tau$ where $i = 0, \ldots, f_s T$, $t_k = kT$ are the GNSS measurement times, and $f_s = \frac{1}{\tau}$. Over any interval $[t_{k-1}, t_k]$, when the context is clear, this notation will be simplified to τ_i. In this notation, $x_{k,i}$ means $x(\tau_{k,i})$, which may be simplified to x_i.

Time propagation of the INS state estimate is the numeric integral of

$$\dot{\hat{x}}(t) = f(\hat{x}(t), \hat{u}(t)) \tag{27}$$

in discrete-time, which is denoted as

$$\hat{x}_i = \phi(\hat{x}_{i-1}, \hat{u}_{i-1}) \tag{28}$$

where $\hat{u}_i = \tilde{u}_i - \hat{b}_u$ and

$$\phi(x_{i-1}, u_{i-1}) = x_{i-1} + \int_{\tau_{i-1}}^{\tau_i} f(x(\tau), u(\tau)) d\tau.$$

Many algorithms are available for the numeric integration [42].

The state vector error propagation model between two IMU time samples can be written as:

$$\delta x_i \doteq \Phi_i \delta x_{i-1} + \gamma_i \omega_i \tag{29}$$

where $\delta x_i = x_i - \hat{x}_i$, $\omega_i \sim \mathcal{N}(0, Q_d)$, and $\Phi_i = \frac{\delta \phi}{\delta x}|_{x_{i-1}, \tilde{u}_{i-1}}$ is the discrete-time INS error state transition matrix. The derivations are contained in [20].

Due to $\tau \ll T$, eqn. (28) is iterated many (i.e. $f_s T$) times between consecutive GNSS measurements. The iterated application of eqn. (28) starts for $i = 0$ with $\hat{x}(\tau_{k-1,0}) = \hat{x}_{k-1}^+$, which is the state estimate after incorporating the GNSS measurements at epoch $k - 1$. The iterated application of eqn. (28) is denoted as

$$\hat{x}_k^- = \phi_k(\hat{x}_{k-1}^+, U_{k-1}) \tag{30}$$

where $U_{k-1} = \{\tilde{u}(\tau_i) \text{ for } \tau_i \in [t_{k-1}, t_k]\}$ denotes the set of IMU measurements over the GNSS epoch. The result of the iterated numeric integration by (28) is the prior $\hat{x}_k^-$ for the extended Kalman filter measurement update at t_k.

The INS error covariance matrix is propagated as

$$P_k^- = \Phi_k P_{k-1}^+ \Phi_k + Q_{d_k} \tag{31}$$

where the derivation and detailed discussion of Q_{d_k} and Φ_k are beyond the scope of this article, but can be found in [43].

B. Measurement Update Model

For both the PVA and INS approaches, the prior state at time t_k will be corrected using the double-differenced pseudorange and Doppler measurements as defined in Section IV-D.

The model for the measurement vector $z_k^s = [\nabla\Delta\rho_k^s, \lambda\nabla\Delta D_k^s]^\top$ for satellite s at t_k is

$$z_k^s \doteq h^s(x_k) + n_k^s, \tag{32}$$

where $n_k^s \sim \mathcal{N}(0, R_z)$ with $h^s(x_k)$ and R_z as defined in eqn. (19). Note that the cross-satellite correlation introduced by the double-difference operation has been ignored.

Based on eqn. (32), the measurement residual is computed as

$$dz_k^s = z_k^s - h^s(\hat{x}_k^-). \tag{33}$$

Employing the first-order Taylor series expansion, the linearized measurement model is:

$$dz_k^s \doteq H_k^s \delta x_k + n_k^s. \tag{34}$$

The following two subsections define the structure of H_k^s based on the definitions of the state vector for the PVA and INS approaches.

Accumulating all satellite measurements dz_k^s into vector dz_k yields:

$$dz_k \doteq H_k \delta x_k + n_k \tag{35}$$

where $dz_k \in \mathbb{R}^{2m}$, H_{d_k} is a matrix with $2m$ rows, and $m + 1$ is the total number of available satellites.

1) PVA Measurement Matrix: For the PVA state vector as defined in eqn. (20), the measurement matrix is

$$H_k^s = \begin{bmatrix} (1_r^s - 1_r^{s_p}) & 0_3 & 0_3 & e_s \\ 0_3 & (1_r^s - 1_r^{s_p}) & 0_3 & 0_m \end{bmatrix}, \quad (36)$$

with $e^s \in \mathbb{R}^{1 \times m}$ being s^{th} row of the identity matrix and 0_j being the zero vector in $\mathbb{R}^{1 \times j}$.

2) INS Measurement Matrix: For the INS state vector as defined in eqn. (24), the error state vector is

$$\delta x = [\delta p^\top, \delta v^\top, \varepsilon, \delta b_a^\top, \delta b_g^\top, \delta M_r]^\top \in \mathbb{R}^{n_e}. \quad (37)$$

where $n_e = 15 + m$. Note that $n_e = n_s - 1$. This is because the quaternion $q \in \mathbb{R}^4$ is a unit vector that only has three degrees-of-freedom. Therefore, the attitude error $\varepsilon \in \mathbb{R}^3$.

The INS measurement matrix is

$$H_k^s = \begin{bmatrix} (1_r^s - 1_r^{s_p}) & 0_3 & 0_9 & e_s \\ 0_3 & (1_r^s - 1_r^{s_p}) & 0_9 & 0_m \end{bmatrix}. \quad (38)$$

C. State Estimation

For the PVA model, state estimation is performed using the linear Kalman filter (KF) [20], [41]. The differential corrections are designed to remove common-mode errors, receiver clock errors are accommodated by double differencing, and multipath is modeled as a state. Details of the KF design and parameter choices are presented in the appendices of [1].

For the INS approach, state estimation is implemented by an extended Kalman filter [20].

VI. EXPERIMENTAL DATA

This section discusses the data and related topics that will be used to generate the experimental results. The experiments analyze the effect of latency on the correction and position accuracy, and the extent to which of different estimation algorithms are able to achieve the one-meter accuracy specification.

A. Data Acquisition

During data acquisition, the hardware is mounted on a sedan that is driven repeatedly along a multi-block section of an urban street (Columbia Ave. near the intersection with Iowa Avenue in Riverside, CA) with low buildings and trees adjacent to the street. The section of street has two stop lights. The trajectory involves two U-turns, one at each end. Therefore, the trajectory involves acceleration and turn rates typical for urban trajectories, which may exceed the variation predicted by the PVA model parameters for short time durations, followed by other trajectory sections where the near constant velocity travel in a lane yields conservative motion relative to that predicted by the PVA model. Selected signals related to the experiment are included as graphs in Appendix A.

The experimental data were saved and post-processed so that multiple algorithms can be compared using identical data. All state estimation results are produced using only pseudo-range and Doppler data. Phase measurements were not used for state estimation.

Raw pseudorange base station data was obtained from a high-quality receiver near Center for Environmental Research

and Technology (CE-CERT) institute in Riverside using the RTCM standard [17] and the NTRIP protocol. The UCR base station had a baseline separation of 2.6 km. The DGNSS correction parameters $[a_{t_0}, b_{t_0}, t_0, IODE]$ are computed and stored (using $L = 500$). This value of L was selected to be about four times the expected base pseudorange multipath correlation time. The DGNSS corrections $c(t; t - \ell)$ will be used at time t to study the impact of the latency ℓ.

This on-vehicle experimental hardware includes two GNSS receivers and one IMU. One receiver is a single frequency u-blox M8T (consumer grade) and the other is dual frequency NOVATEL OEMV2 (survey grade). Both receivers are connected to the same Antcomm ANN-MS-0-005 antenna. The M8T single-frequency receiver provides GNSS data for state estimation for both the PVA and INS approaches. The INS implementation also used inertial measurement data. The IMU on the vehicle was an NV-IMU 1000, which is a navigation-grade sensor. Before using the data for analysis, it will be processed (see Appendix B) to produce IMU data characteristic of a consumer-grade IMU.

The experiment lasted 1800 seconds. During the first 500 seconds, the base station is accumulating its $L = 500$ second buffer. Therefore, the data available for performance analysis is 1300 s.

The OEMV2 receiver provided more accurate (two frequency code and carrier) data for (smoothed) estimation of a ground truth trajectory enables analysis of the state estimation accuracy on a moving platform.

B. Ground Truth Trajectory

Ground truth trajectory estimation was performed in post-processing using a Maximum a Posteriori smoothing algorithm [44]. It used the two-frequency pseudorange and integer-resolved, carrier phase GNSS data from the OEMV2 and NV-IMU 1000 to achieve centimeter accuracy. This ground truth trajectory and OEMV2 data are only used to assess the accuracy of the state estimation results from the consumer-grade receiver and IMU.

C. Position Estimation Scenarios

The following subsections report positioning accuracy for two estimation scenarios, see Section V:

1) **PVA** will use only the M8T GNSS data with a Linear KF to estimate the state defined in eqn. (20) using double-difference pseudorange and Doppler measurements.
2) **INS (Consumer-grade IMU)** uses the M8T GNSS and IMU data (corrupted to have performance similar to the ADIS16360, see Section VI-E and Appendix A). The IMU data is integrated through an INS to produce the state vector defined in eqn. (24). The INS error state, defined in eqn. (37), is estimated with an EKF using double-difference pseudorange and Doppler measurements.

Each algorithm processes the set of GNSS measurements ($k = 1, \ldots, N_d$) as if they were occurring in real-time (i.e., incrementally) to estimate the state vector at each time k, using

correction $\hat{c}(k;k-l)$ from eqn. (9) for a given value of the latency l. The symbol $\hat{p}^a_{k,l}$ denotes the position estimated for time k for scenario $a \in \{1,2\}$ for corrections with lag ℓ.

The norm of horizontal position error at time k for scenario a and latency ℓ is

$$e^a_{h_{k,l}} = \left\| \begin{bmatrix} 1 & 0 & 0 \\ 0 & 1 & 0 \end{bmatrix} \left(p_{r_k} - \hat{p}^a_{k,l} \right) \right\| \tag{39}$$

where p_{r_k} is the post-processed (i.e., smoothed) ground truth position. This error is calculated using the posterior state estimate. The vertical position error $e^a_{v_{k,l}}$ is defined similarly using only the third (i.e., down) position component. This equation assumes that all position vectors are represented in the North-East-Down navigation frame.

D. Outlier Accommodation

Outlier detection is implemented by applying a Neyman Pearson (NP) test [45] to each element of the measurement residual vector dz_k. Residuals are only used in the (E)KF if they pass the test $|dz^s_k| \le \gamma_o \sigma^s_k$ where $z^s_k \sim N(0, \sigma^s_k)$. The symbol σ^s_z is the residual standard deviation as computed within the (E)KF algorithm and γ_o is a user defined threshold. Unless otherwise stated, $\gamma_o = 1$. Performance in the presence of outliers as a function of γ will be considered in Section IX.

E. Consumer-Grade IMU Measurements

One of the main purposes of this study is to show positioning performance using consumer-grade sensors. The IMU sensor that has been used in this experiment (NV-IMU 1000) is much better than consumer-grade.

To analyze navigation performance for a consumer-grade IMU the NV-IMU 1000 data is corrupted with additive stochastic errors corresponding to the specification of the ADIS16360 IMU from Analog Device. The stochastic error generation methodology is described in Appendix B.

VII. POSITIONING ACCURACY WITHOUT LATENCY

Fig. 1 shows histograms of $e^a_{h_{k,l}}$ as defined in eqn. (39) for latency $l = 0$ for each scenario summarized in Section VI-C. Both plots are generated using $N_d = 1300$ epochs error data.

Table Ia and Ib summarize various measures of positioning accuracy (for latency $l = 0$) for horizontal (e_h) and vertical (e_v) error, respectively. Column 1 shows the scenario number a. Column 2 displays the mean position error. Column 3 contains the standard deviation of the position error. Column 4 shows the maximum value of the position error. Columns 5 and 6 report the percentage of samples that have a positioning error less than the accuracy specified in the column header. Results shown in the statistics were computed over $N_d = 1300$ seconds.

Both the histogram and the table shows that both the PVA and the INS performance exceed the SAE standard [12]. As expected, the INS, which has more information, performs better than the PVA approach. The PVA approach (i.e., Scenario 1) achieves meter-level horizontal position accuracy at 90%. The INS approach using the consumer grade IMU (i.e., Scenario 2) achieves meter-level accuracy at 98% and two-meter accuracy at 100%.
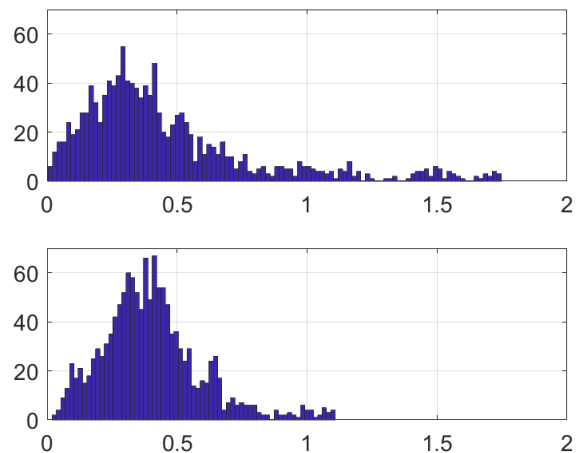

Fig. 1: Histogram of horizontal position error $e^n_{h_{k,l}}$ defined in eqn. (39) with $l = 0$ for PVA approach (Top) and INS with consumer-grade IMU (Bottom).

The INS performance herein is similar to that reported in [1] for a stationary receiver, which is as it should be, because the purpose of the INS to remove the effects of motion on the performance by using the IMU data. Due to the small eigenvalues of the INS error model, the IMU sensor errors slowly accumulate. This accumulation is independent of vehicle motion. The EKF estimates and corrects the INS error state using the double-difference GNSS measurements.

VIII. EXPERIMENTAL RESULTS: LATENCY EFFECTS

This section analyzes the effect of DGNSS communication latency on positioning error.

A. Correction Sensitivity to Latency

The correction error at epoch k due to communication latency l, as defined in eqn. (11), is

$$e_c(k,l) = |\hat{c}(k;k) - \hat{c}(k;k-l)|, \tag{40}$$

where $\hat{c}(k;k)$ is the correction with no latency and $\hat{c}(k;k-l)$ is the correction with latency of l epochs. Both corrections are computed using eqn. (9). Statistics related to $e_c(k,l)$ are computed by averaging over $k = 1, \ldots, N_d$.

Fig. 2a shows the mean plus and minus the standard deviation of $e_c(k,l)$ versus l for three satellites. For each fixed value of l and each satellite, the mean and standard deviation of $e_c(k,l)$ are computed from experimental data by averaging over N_d epochs. Fig. 2a shows that the correction error $e_c(k,l)$ remains less than one meter for more than $\ell = 500 secs$.

B. Position Estimation: Sensitivity to Latency

The experiment is repeated for each scenario $a \in \{1,2\}$ and each latency $l \in \{0, \ldots, 800\}$ seconds. Each experiment produces a position sequence $\hat{p}^a_{k,l}$ for $k = 1, \ldots, N_d$.

For each of the two scenarios, Fig. 2b illustrates the effect of the DGNSS correction latency l on the GNSS position accuracy as measured by $e^a_{h_{k,l}}$ defined in eqn. (39). For each
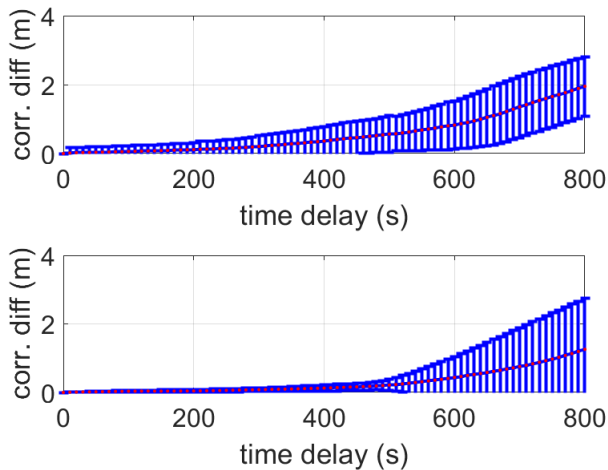
TABLE I: Positioning Performance without communication latency (e.g., $l = 0$).

(a) Horizontal Error Statistics.

Scenario	Mean	Std. Dev	Max	Prob.	
				$e^a_{h_{k,0}} < 1m$	$e^a_{h_{k,0}} < 2m$
1. PVA	0.46	0.34	1.7	90	100
2. CG-INS	0.40	0.18	1.1	98	100

(b) Vertical Error Statistics.

Scenario	Mean	Std. Dev	Max	Prob.	
				$e^a_{v_{k,0}} < 2$	$e^a_{v_{k,0}} < 3$
1. PVA	0.98	0.70	4.4	95	98.2
2. CG-INS	1.03	0.56	3.2	95	99.7

(a) Correction error defined in eqn. (40) versus latency for two satellites for $N_d = 1000$ epochs.
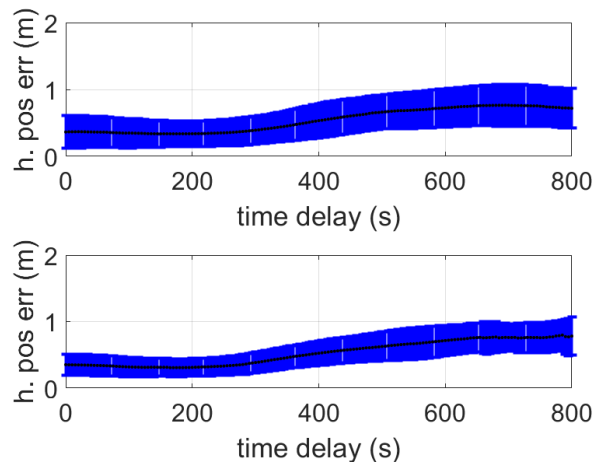
(b) Horizontal position error vs latency for $N_d = 500$ epochs. GNSS aided PVA model (Top). GNSS aided INS with consumer-grade IMU (Bottom).

Fig. 2: Error sensitivity to latency ℓ

graph, the black curve shows the mean of $e^a_{h_{k,l}}$ averaged over k, for a fixed value of a, versus ℓ. Each point on the graph is also marked with a one-standard-deviation error bar that is indicated in blue. From Fig. 2b, the mean and standard-deviation of the horizontal position error for the PVA approach are larger than for the INS approach as a function of latency. Both scenarios in Fig. 2b show that position estimation accuracy is insensitive to communication latency in the sense that it is able to achieve one meter accuracy at the 1-σ level for latencies exceeding $\ell = 500$ secs.

IX. EXPERIMENTAL RESULTS: POSITION ACCURACY IN THE PRESENCE OF OUTLIERS

This section shows the effects of outliers on positioning performance. The dataset is the same as described for Section VI-A, only the duration has been decreased to $N_d = 300$ seconds to reduce the required computational cost of the Monte Carlo simulations.

A. Outlier Generation for GNSS Measurement

The environment where the car was driven for this experiment was selected to have a clear sky – only a few large trees and one or two storied buildings. Therefore the collected data set should be essentially outlier-free. This was confirmed by analyzing the KF residuals. The average number of GNSS measurements per epoch over the entire trajectory was 8.

The fact that the data set is outlier-free allows the effect of outliers to be analyzed in a sequence of Monte Carlo experiments, by artificially inserting outlier measurements. To maintain consistency in performance, the same outlier corrupted data is used for all algorithms at each Monte Carlo run.

For each epoch of each Monte Carlo experiment, computer-generated outliers are added to two randomly chosen satellites. The size of each outlier is drawn from a uniform distribution parameterized by μ. For $\mu < 1.5$, the distribution is $U[0, \mu + 1.5]$. For $\mu >= 1.5$, the distribution is $U[\mu - 1.5, \mu + 1.5]$. Each Monte Carlo experiment has a fixed value of μ for N_M trials. Each trial lasts for N_d seconds. Each trial of each experiment uses a different random seed.

For each trial, all three algorithms will all use the same data, with the same outlier corruption, so that performance can be compared.

The different Monte Carlo experiments each use a different value of $\mu \in [0.2, 20]$ to create the performance curves versus α. Each point on each curve is produced as the average of horizontal position error over the N_d seconds and N_M trials.

B. Outlier Rejection Criteria

For each measurement, the (E)KF computes both the residual and its covariance: $\sigma^2_{ii} = \sqrt{R_{ii} + h_i P^-_k h_i^\top}$ where h_i is the ith row of H. Per the NP outlier rejection test, a measurement is only used if the absolute value of the residual is less than $\gamma \sigma_{ii}$;

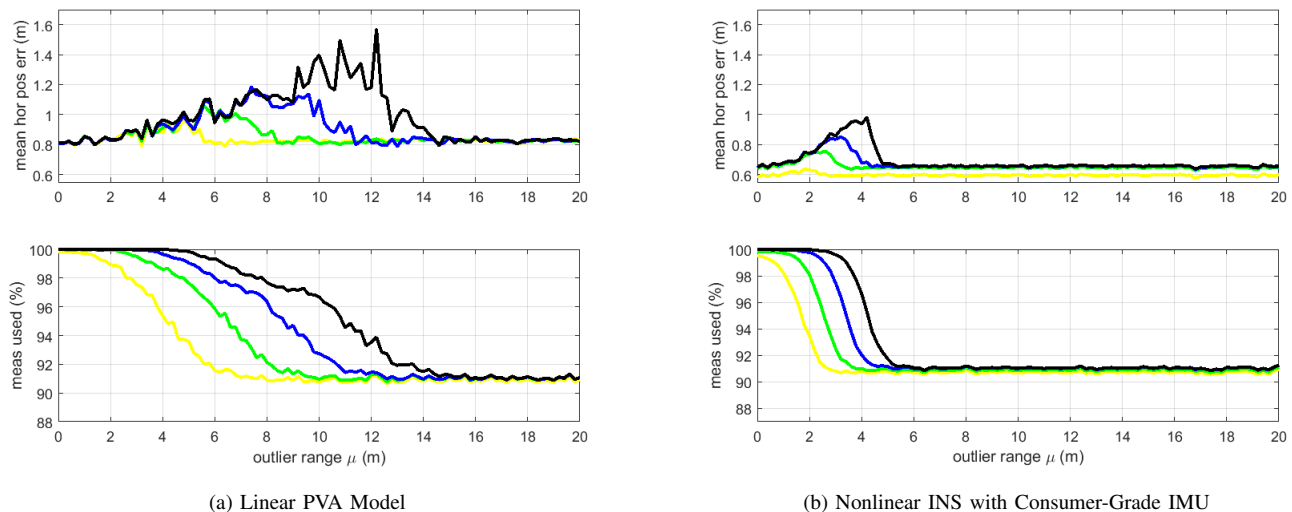(a) Linear PVA Model   (b) Nonlinear INS with Consumer-Grade IMU

Fig. 3: Mean horizontal position error and the percentage of selected measurements versus mean outlier magnitude $\mu \in [0,20]$. The yellow, green, blue and black curves show the results for the NP-(E)KF approach with $\gamma =2$, 3, 4, and 5, respectively.

otherwise it is ignored. Performance will be evaluated for the different values: $\gamma = 2, 3, 4, 5$. A typical value in applications is $\gamma = 3$.

C. Performance Analysis in the Presence of Outliers

Figs. 3a and 3b show the performance of the GNSS aided PVA (left) and GNSS aided INS (right) approaches as a function of the outlier magnitude μ. Each color of curve corresponds to a distinct value of γ for the NP-(E)KF residual test as defined in the caption. The *x*-axis is the parameter μ, which is the mean outlier magnitude for a Monte Carlo experiment. The *y*-axis in each top sub-figure is the mean horizontal position error. The *y*-axis in each bottom sub-figure is the percentage of measurements used on average. At each time instant, the measurement set (pseudorange and Doppler) contains 9% generated outliers.

For both the PVA and INS approaches, the mean horizontal position error initially rises as μ increases beyond about 1 m, because small outliers are difficult to discriminate from measurement noise. As μ continues to increase, the mean horizontal position error for each curve eventually decreases. This is because large magnitude outliers are reliably rejected by the NP test. The magnitude of μ at which this occurs is a function of the test decision threshold γ. The trade-off is that smaller values of γ due a better job of rejecting outliers, but have a higher risk of rejecting valid measurements (i.e. false alarms). Correct rejection of all outliers occurs for smaller values of μ as the NP threshold γ decreases.

The INS has both more information (i.e., IMU data) and a more accurate propagation (though nonlinear) model. The result is that the GNSS-INS approach yields measurement residuals and error covariance matrix P_k^- that are smaller than the GNSS-PVA approach. Therefore, the NP-EKF tests are able to detect and remove outliers at significantly smaller val-

ues (i.e., for $\gamma = 5$, μ equal to 5.4 for GNSS-INS versus 14.4 for GNSS-PVA).

X. CONCLUSION AND FUTURE WORK

Real-time absolute positioning (i.e., relative to an Earth frame) is one of the primary requirements of navigation technology in important commercial applications, e.g. connected and autonomous vehicles. Data communication latency, interruption, and lost packets are the challenges that all real-time systems encounter. Reliably achieving submeter position accuracy in realistic environments on moving platforms is a main focus of this research project.

The purpose of the studies presented herein was to evaluate the ability to achieve SAE position accuracy specifications on moving platforms in natural environments. Section IV discussed GNSS measurement error characteristics and methods to accommodate them. That section reviewed a DGNSS correction algorithm designed to compensate latency, short-term communication interruption, and lost packets [1], [2]. Section V presented the PVA and INS estimation algorithms that were studied herein. The PVA and INS approaches both augmented one multipath state per satellite and used Doppler measurements along with pseudorange, to enhance the degree-of-observability as well as positioning performance.

The results herein demonstrated that: (1) with suitable algorithmic processing, positioning performance is insensitive to correction latency up to 500 s; and (2) horizontal position estimation accuracy is achievable at the submeter level for over 98% of samples using a consumer-grade IMU and for over 90% of samples using the PVA approach. All results herein used data acquired in an environment with relatively clear sky (no obstacles). Surfaces the block, obstruct, or corrupt the GNSS signals will affect the results. The PVA performance will be trajectory dependent, while the INS approach should be relatively robust to the nature of the trajectory, assuming

the measured signals are within the IMU bandwidth and range specifications.

Topics of additional research interest include extending the results herein to real-time implementations; and, inclusion of carrier phase measurements [20], multiple frequencies (L2, L5), and multiple constellations (e.g., Galileo, BeiDou, QZSS, IRNSS) [46]–[49]. Also of interest is the use and study of network differential GNSS.

XI. ACKNOWLEDGEMENT

APPENDIX

A. Test Trajectory

This section provides graphs of various signals to allow the reader to understand the nature of the test trajectory. The data in this section is the ground truth data that is the output of the post-processed trajectory smoother. See Section VI-B.

During data collection the sensor equipped car was driven predominantly in the east-west direction. At each end of the test area, the vehicle took a U-turn. This round trip traverse was repeated four times. U-turns, traffic signals, and other traffic necessitated angular rates and accelerations that are measured by the IMU and incorporated in the INS approach, but that may violate the assumptions inherent in the PVA approach.

Fig. 4 shows the horizontal trajectory using a graph of the east versus north position estimates. The black and red dots are showing the start and end point. The same trajectory is overlaid on a Google Earth map in Fig. 5. The red dots indicate the car position.

Fig. 6 shows the body-frame X and Y axis (i.e. horizontal) acceleration data. The figure shows that nearly 1-g acceleration is experienced routinely.
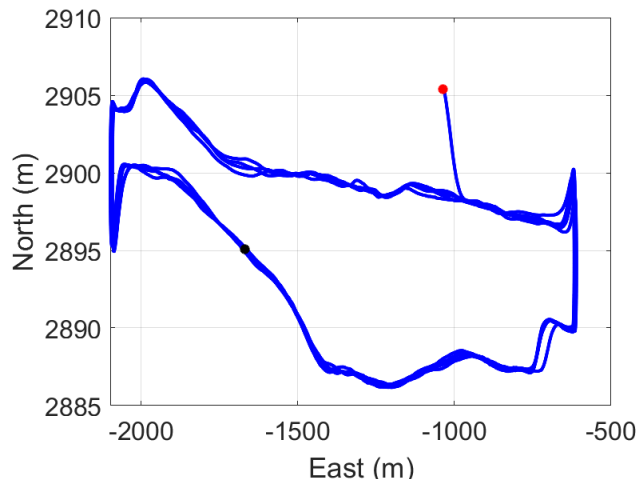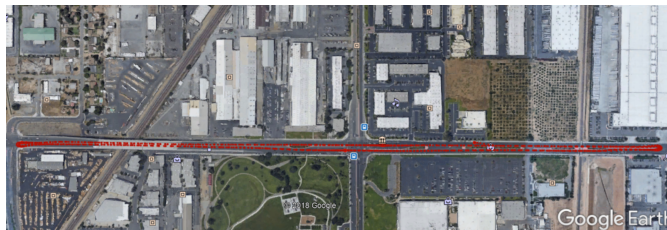

Fig. 5: Trajectory overlaid on a Google Earth map. The data is collected on Columbia Ave. The cross street near the center is Iowa Ave.
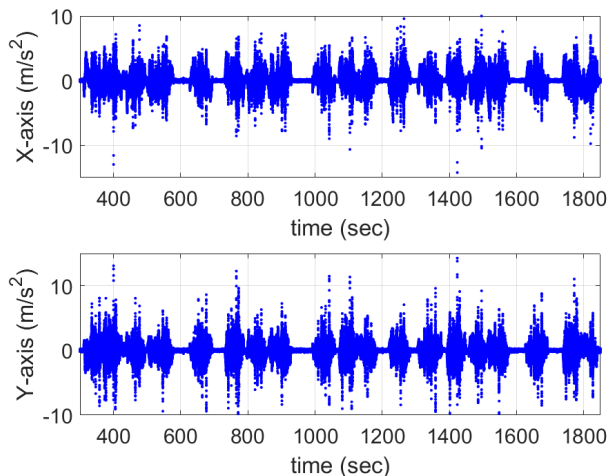

Fig. 6: Horizontal body frame acceleration.

Fig. 7 shows the angular rate data. The times at which the large magnitude yaw angular rate measurements occur indicates the times at which the U-turns occurred.
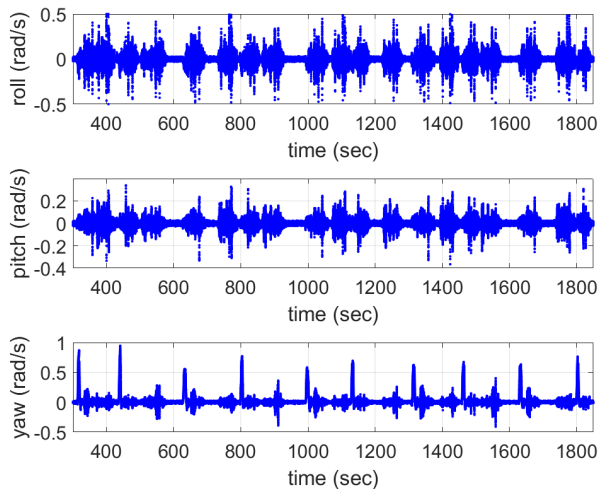

Fig. 7: Angular rate plot.

Fig. 4: North east trajectory plot.

B. Consumer-Grade IMU Error Model

This section describes the state space model design to generate noise with characteristics for a consumer-grade IMU. This model is used to create IMU measurement errors that are added to the measurements of the navigation-grade IMU to test the performance for a consumer-grade IMU.

For a consumer grade IMU, the primary noise sources are:

- Angle/velocity random walk, parameterized by the coefficient N;
- Bias instability, parameterized by the coefficient B and correlation time T_B;
- Rate/acceleration random walk, parameterized by the coefficient K.

The parameters N, B, K, and T_B are either provided by the data sheet or read from the Allan Variance (AV) plot, depending what is provided by the manufacturer.

1) Sensor Model: The continuous-time sensor measurement model is

$$\tilde{u}(t) = (1+s_f)u(t) + z(t) \tag{41}$$

where $u(t)$ is the true signal and $\tilde{u}(t)$ is the measured signal, s_f is the scale factor error and $z(t)$ represents stochastic errors. In this study, deterministic errors such as s_f are ignored. The model for $z(t)$ has three terms

$$z(t) = z_N(t) + z_B(t) + z_K(t) \tag{42}$$

where $z_N(t)$, $z_B(t)$ and $z_K(t)$ are the mutually independent stochastic errors associated with coefficients N, B, and K, respectively.

For the results herein, the experimental data was collected with a navigation-grade sensor (i.e., NV IMU-1000 from Nav Technology). Our goal was to test navigation results for a consumer-grade IMU, but we did not have access to such sensors. To produce data corresponding to a consumer-grade IMU, the NV IMU-1000 experimental data will serve as u, which will be corrupted by stochastic error $z(t)$ produce in simulation to produce $\tilde{u}$ corresponding to the performance of the ADIS16360 consumer-grade sensor, which has the following stochastic error specifications $N = 0.0037$ m/s/$\sqrt{s}$, $B = 0.00301$ m/ s^2, $K = 0.00078$ m/s/$s^{3/2}$ and $T_B = 25$s as read from the Allan standard deviation plot on the data sheet.

2) State Space Model: Because the Power Spectral Densities (PSD) of $z(t)$ is not an even function of frequency, there is not a unique state-space model that will produce $z(t)$. Any state space model is an approximation.

The state-space model used herein is

$$\dot{x}_z(t) = A x_z(t) + B \omega(t), \tag{43}$$
$$z(t) = C x_z(t) + \eta(t). \tag{44}$$

The state-space matrices are

$$A = \begin{bmatrix} -\mu_B & 0 \\ 0 & 0 \end{bmatrix}, \quad B = \begin{bmatrix} 1 & 0 \\ 0 & 1 \end{bmatrix}, \quad C = \begin{bmatrix} 1 & 1 \end{bmatrix}, \tag{45}$$

where $\mu_B = \frac{1}{T_B}$. The state vector is $x_z(t) = \begin{bmatrix} z_B(t), & z_K(t) \end{bmatrix}^\top$. The driving noise input $\omega(t) = \begin{bmatrix} \omega_B(t), & \omega_K(t) \end{bmatrix}^\top$ and measurement noise $\eta(t)$ are mutually independent Gaussian white noise processes. The PSD of $\omega(t)$ is

$$Q_z = \begin{bmatrix} Q_B & 0 \\ 0 & Q_K \end{bmatrix} \tag{46}$$

where $Q_B = \frac{2B^2 \ln(2)}{\pi (0.4365)^2 T_B}$ and $Q_k = K^2$. The PSD of $\nu(t)$ is $Q_\eta = N^2$, respectively.

The IMU measurements occur in discrete-time with a sampling period of $T = 0.005$ seconds. For this sample period, using the parameters for the ADIS16360 sensor and the notation $z(k) = z(kT)$, the discrete-time consumer grade IMU error model is

$$x_z(k) = \Phi x_z(k) + \omega_z(k), \tag{47}$$
$$z(k) = C x_z(k) + \eta(k) \tag{48}$$

where $\omega_{z_k} \sim N(0, Q_{z_d})$ is a random two-dimensional Gaussian vector and $\eta_k \sim N(0, Q_{\eta_d})$ is a random Gaussian scalar variable.

The discrete-time state transition matrix Φ and matrix $Q_{z_d} = cov(\omega_z(k))$ are computed from A and Q_z using the method in Chapter 4.7 in [20]. The relationship between continuous-time PSD Q_η and discrete-time covariance $Q_{\eta_d} = cov(\eta(k))$ is:

$$Q_{\eta_d} = \frac{Q_N}{T}. \tag{49}$$

Factoring $Q_{z_d} = \Sigma_\omega \Sigma_\omega^\top$, then samples of the process noise can be computed as $\omega_z(k) = \Sigma_\omega v(k)$ where $v(k) \sim N(0, I)$ is a standard two-dimensional Gaussian random vector. Factoring $Q_{\eta_d} = \sigma_{\eta_d}^2$, samples of the measurement noise can be computed as $\omega_z(k) = \sigma_{\eta_d} w(k)$ where $w(k) \sim N(0, 1)$ is a standard Gaussian random variable. The variables $v(k)$ and $w(k)$ are easily computed in simulation.

This discrete-time measurement error $z(k)$ is computed using eqns. (47-48). The consumer-grade IMU measurements are computed using eqn. (41).

REFERENCES

[1] F. Rahman, E. Aghapour, and J. A. Farrell, "ECEF Position Accuracy and Reliability in the Presence of Differential Correction Latency Year 1 Technical Report for Sirius XM," University of California, Riverside, Tech. Rep., October, 2018. [Online]. Available: escholarship.org/uc/item/38d3h08w

[2] ——, "ECEF Position Accuracy and Reliability in the Presence of Differential Correction Latency," *IEEE/ION PLANS*, 2018.

[3] E. Aghapour, F. Rahman, and J. A. Farrell, "Risk-averse performance-specified state estimation," *IEEE/ION PLANS*, 2018.

[4] G. Blewitt, "Basics of the GPS Technique: Observation Equations," *Geodetic applications of GNSS*, pp. 10–54, 1997.

[5] C. Shuxin, Y. Wang, and C. Fei, "A study of differential GNSS positioning accuracy," *in 3rd Int. Conf. on Microwave and Millimeter Wave Tech.*, pp. 361–364, 2002.

[6] P. Misra and P. Enge, "Special issue on global positioning system," *IEEE*, vol. 87, no. 1, pp. 3–15, 1999.

[7] B. Hofmann-Wellenhof, H. Lichtenegger, and J. Collins, *"Global Positioning System: Theory and Practice"*. Springer Science & Business Media, 2012.

[8] C. Basnayake, M. Joerger, and J. Auld, "Safety-Critical Positioning for Automotive Applications: Lessons from Civil Aviation," Tech. Rep., November, 2016. [Online]. Available: http://insidegnss.com/assets/webinar/201611/Inside-GNSS-Webinar_Safety-Critical-Positioning-for-Automotive-20161103.pdf

[9] F. M. Kitchener, T. English *et al.*, "Connected Vehicle Pilot Deployment Program Phase 2, Data Management Plan-Wyoming." USDOT, Tech. Rep., April, 2017. [Online]. Available: https://transportationops.org/publications/connected-vehicle-pilot-deployment-program-phase-2-data-management-plan-wyoming-dot

[10] S. Cadzow *et al.*, "Connected Vehicle Pilot Deployment Program Phase 2: Data Privacy Plan-New York City." USDOT, Tech. Rep., December, 2016. [Online]. Available: https://rosap.ntl.bts.gov/view/dot/32311

[11] S. Johnson, L. Rolfes *et al.*, "Connected Vehicle Pilot Deployment Program Phase II Data Privacy Plan-Tampa (THEA)." USDOT, Tech. Rep., February, 2017. [Online]. Available: https://rosap.ntl.bts.gov/view/dot/32763

[12] Anonymous, "On-Board System Requirements for V2V Safety Communications," Tech. Rep., March, 2016. [Online]. Available: https://saemobilus.sae.org/content/j2945/1_201603

[13] P. Teunissen and O. Montenbruck, *Handbook of Global Navigation Satellite Systems*. Springer, 2017, vol. 26(2).

[14] M. S. Braasch and A. Van Dierendonck, "GPS receiver architectures and measurements," *Proc. of the IEEE*, vol. 87(1), pp. 48–64, 1999.

[15] P. Misra and P. Enge, "Global Positioning System: Signals, Measurements and Performance, second edition," *Massachusetts: Ganga-Jamuna Press*, 2006.

[16] B. W. Parkinson, J. Spilker, and P. Enge, "Global Positioning System: Theory and Applications," *AIAA*, vol. 2, pp. 3–50, 1996.

[17] Anonymous, "RTCM Standard 10403.2 for Differential GNSS (Global Navigation Satellite Systems) Services," RTCM Special Committee, Tech. Rep., August, 2001.

[18] P. K. Enge, R. M. Kalafus, and M. F. Ruane, "Differential operation of the global positioning system," *IEEE Comm. Mag.*, vol. 26(7), pp. 48–60, 1988.

[19] P. Teunissen, "Differential GPS: Concepts and Quality Control," *Netherlands Institution of Navigation, Amsterdam*, 1991.

[20] J. A. Farrell, *"Aided Navigation: GNSS with High Rate Sensors"*. McGraw-Hill Inc, 2008.

[21] P. Enge, "The global positioning system: Signals, measurements, and performance," *Int. J. of Wireless Info. Net.*, vol. 1(2), pp. 83–105, 1994.

[22] M. S. Grewal, L. R. Weill, and A. P. Andrews, *"Global Positioning System, Inertial Navigation,and Integration"*. John Wiley & Sons, 2007.

[23] Y. Saber, R. Antri-Bouzar, M. Sebeloue, and J. Boucher, "Comparison between two navigation modes for differential GPS," *IEEE Microwave and Millimeter Wave Tech. Conf.*, pp. 463–466, 1998.

[24] P. Loomis, G. Kremer, and J. Reynolds, "Correction algorithms for differential GPS reference stations," *Navigation*, vol. 36(2), pp. 179–193, 1989.

[25] G. T. Kremer, R. M. Kalafus, P. V. Loomis, and J. C. Reynolds, "The effect of selective availability on differential GPS corrections," *Navigation*, vol. 37, no. 1, pp. 39–52, 1990.

[26] J. A. Farrell, M. Grewal, M. Djodot, and M.Barth, "Differential GNSS with latency compensation for autonomous navigation," *Int. Symp. on Int. Cont.*, pp. 20–24, 1996.

[27] J. A. Farrell, M. Djodat, M. Barth, and M. Grewal, "Latency compensation for differential GPS," *Navigation*, vol. 44(1), pp. 99–107, 1997.

[28] B. Townsend and P. Fenton, "A practical approach to the reduction of pseudorange multipath errors in a L1 GPS receiver," *7th Int. Tech. Meeting of the Sat. Div. of the ION*, 1994.

[29] F. Lee, S. Chun, Y. J. Lee, T. Kang, G. Jee, and J. Kim, "Parameter estimation for multipath error in GPS dual frequency carrier phase measurements using unscented Kalman filters," *Int. J. of Cont., Auto., and Sys.*, vol. 5(4), pp. 388–396, 2007.

[30] J. K. Ray, *"Mitigation of GPS Code and Carrier Phase Multipath Effects Using a Multi-Antenna System"*. University of Calgary, 2000.

[31] J. M. Tranquilla, J. Carr, and H. M. Al-Rizzo, "Analysis of a choke ring groundplane for multipath control in global positioning system (GPS) applications," *IEEE T. on Ant. and Prop.*, vol. 42(7), pp. 905–911, 1994.

[32] L. Serrano, D. Kim, R. B. Langley, K. Itani, and M. Ueno, "A GPS velocity sensor: how accurate can it be?–a first look," *ION NTM*, vol. 2004, pp. 875–885, 2004.

[33] L. Serrano, D. Kim, and R. B. Langley, "A single GPS receiver as a real-time, accurate velocity and acceleration sensor," *17th Int. Tech. Meeting of the Sat. Div. of ION*, vol. 2124, 2004.

[34] M. D. Agostino, A. Manzino, and G. Marucco, "Doppler measurement integration for kinematic real-time GPS positioning," *Applied Geomatics*, vol. 2(4), pp. 155–162, 2010.

[35] J. An and J. Lee, "Improvement of GPS position estimation using SNR and Doppler," *in IEEE Int. Conf. on AIM*, pp. 1645–1650, 2017.

[36] G. Lachapelle, "GNSS observables and error sources for kinematic positioning," *Kinematic Systems in Geodesy, Surveying, and Remote Sensing*, pp. 17–26, 1991.

[37] C. Kee, B. W. Parkinson, and P. Axelrad, "Wide area differential GPS," *Navigation*, vol. 38(2), pp. 123–145, 1991.

[38] P. Enge, T. Walter, S. Pullen, C. Kee, Y.-C. Chao, and Y.-J. Tsai, "Wide area augmentation of the global positioning system," *IEEE*, vol. 84(8), pp. 1063–1088, 1996.

[39] J. Zumberge, M. Heflin, D. Jefferson, M. Watkins, and F. H. Webb, "Precise point positioning for the efficient and robust analysis of gps data from large networks," *J. of geophysical research: solid earth*, vol. 102(B3), pp. 5005–5017, 1997.

[40] J. Kouba and P. Héroux, "Precise point positioning using IGS orbit and clock products," *GPS solutions*, vol. 5(2), pp. 12–28, 2001.

[41] R. Brown and P. Hwang, *"Introduction to Random Signals and Applied Kalman Filtering"*. Wiley, New York, 1996.

[42] P. J. Davis and P. Rabinowitz, *"Methods of numerical integration"*. Courier Corporation, 2007.

[43] P. F. Roysdon and J. A. Farrell, "Technical Note: INS Noise Propagation," Tech. Rep., October, 2018. [Online]. Available: escholarship.org/uc/item/33x8t208

[44] A. Vu, J. A. Farrell, and M. Barth, "Centimeter-accuracy smoothed vehicle trajectory estimation," *IEEE Intel. Transp. Sys. Mag.*, vol. 5(4), pp. 121–135, 2013.

[45] J. Neyman and E. S. Pearson, "The testing of statistical hypotheses in relation to probabilities a priori," *Cambridge University Press*, pp. 492–510, 1933.

[46] R. Odolinski, P. Teunissen, and D. Odijk, "An analysis of combined COMPASS/BeiDou-2 and GPS single-and multiple-frequency RTK positioning," *ION Pacific PNT*, pp. 69–90, 2013.

[47] N. Nadarajah, A. Khodabandeh, and P. J. Teunissen, "Assessing the IRNSS L5-signal in combination with GPS, Galileo, and QZSS L5/E5a-signals for positioning and navigation," *GPS solutions*, vol. 20(2), pp. 289–297, 2016.

[48] D. Odijk, N. Nadarajah, S. Zaminpardaz, and P. J. Teunissen, "GPS, Galileo, QZSS and IRNSS differential ISBs: estimation and application," *GPS solutions*, vol. 21(2), pp. 439–450, 2017.

[49] M. Choi, J. Blanch, D. Akos, L. Heng, G. Gao, T. Walter, and P. Enge, "Demonstrations of multi-constellation advanced RAIM for vertical guidance using GPS and GLONASS signals," *ION GNSS*, pp. 3227–3234, 2011.